Geophys. J. Int. (2004) **157,** 727–736 doi: 10.1111/j.1365-246X.2004.02220.x

The 1995 Kozani–Grevena (northern Greece) earthquake revisited: an improved faulting model from synthetic aperture radar interferometry

Alexis Rigo,[1] Jean-Bernard de Chabalier,[2] Bertrand Meyer[3] and Rolando Armijo[3]

[1] *Observatoire Midi-Pyrénées, UMR* 5562, *CNRS - University Paul Sabatier,* 14 *Avenue Edouard Belin,* 31400 *Toulouse, France. E-mail: Alexis.Rigo@cnes.fr*
[2] *Institut de Physique du Globe, CNRS-UMR* 7580, 4 *Place Jussieu,* 75252 *Paris Cedex* 05, *France*
[3] *Institut de Physique du Globe, CNRS-UMR* 7578, 4 *Place Jussieu,* 75252 *Paris Cedex* 05, *France*

Accepted 2003 December 9. Received 2003 November 27; in original form 2002 August 1

SUMMARY

Previously, geodetic data associated with earthquakes have been widely modelled using co-planar rectangular dislocations in an elastic half-space. However, such models appear inadequate when complex geometries such as variations in strike and dip or multiple fault segments are involved. Here we revisit the 1995 $M_s = 6.6$ Kozani–Grevena earthquake, and use synthetic aperture radar (SAR) interferometric measurements, tectonic observations and seismological data to constrain a fault model with a realistic geometry. We undertake a critical analysis of all available SAR data, including characterization of atmospheric artefacts. These are partially removed and the possibility that such effects are misidentified as secondary faulting is examined. Three well-correlated interferograms provide an accurate and complete description of the ground deformation field associated with the event. To take into account the complexity of the fault system activated during the earthquake, we construct a 3-D fault model, composed of triangular elements, that is geometrically more consistent with surface ruptures than those of previous studies. Using first trial-and-error and then iterative inversion, we explore the ranges of geometric parameters that can explain the data. We obtain an average final model and its standard deviation, with small slip amplitude at the surface, consistent with the field observations, and with slip as large as 2.5 m at depth. This model is compared with those previously published. We conclude that an antithetic fault is not required to explain the SAR data.

Key words: fault models, inversion, normal faulting, satellite geodesy, seismotectonics.

1 INTRODUCTION

Maps of surface co-seismic deformation fields obtained by analysis of interferometric synthetic aperture radar (InSAR) images have significantly improved the description of earthquake source mechanisms. The high spatial sampling density (more than 100 measurements per km^2) and the high precision (a few mm) allow the detection of very subtle deformations inaccessible to other geodetic techniques, as long as the images remain correlated (no drastic changes of surface conditions, no excessive gradients of deformation) over the time interval covered by the interferogram. It is now possible to determine with confidence the detailed geometry and the distribution of slip on a fault system activated during an earthquake (for example, Feigl *et al.* 1995; Hernandez *et al.* 1999; Feigl *et al.* 2002), the interseismic loading (for example, Wright *et al.* 2001), the post-seismic relaxation (for example, Massonnet *et al.* 1994) and the possible spatial and temporal variations of the mechanical behaviour of the crust (Peltzer *et al.* 1998). However, the displacement field measured at the surface is interpreted in terms of a rupture mechanism that takes place at depth. Because of the large number of free parameters, inversions suffer from intrinsic problems: solutions are non-unique and unstable due to trade-offs between parameters. Thus, it is essential to consider other observations and to fix some known parameters such as surface ruptures, geometry of faults consistent with geology, the location of the hypocentre or the aftershock distribution. To take advantage of the information given by these data, the approaches and the models must be allowed to evolve. In most cases, faults are simplified and represented by co-planar rectangular dislocations embedded in an elastic half-space; the complexity of faults, as represented by changes in strike, step over, or the existence of *en echelon* segments, is smoothed out, and assumed as of second order.

For all these reasons, the study of the Kozani–Grevena earthquake in northern Greece is of particular interest. On 1995 May 13, Kozani and Grevena were struck by an $M_s = 6.6$ earthquake, causing extensive damage. Using local seismological data and a strong motion record, Hatzfeld *et al.* (1997) relocated the main shock at 40.183°N and 21.660°E with a precision of 2 km, beneath the Vourinos mountains at a depth of 14.2 ± 2.4 km (Fig. 1). The overall structure and morphology of this region is well known (Meyer *et al.* 1996).

© 2004 RAS

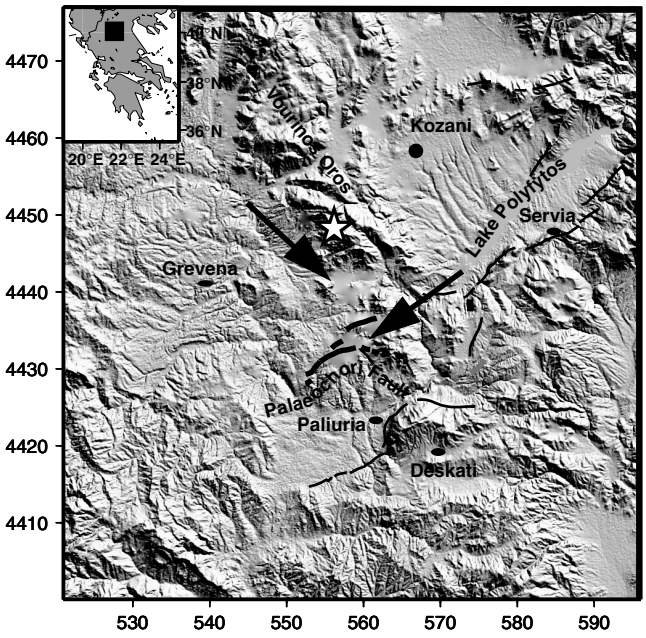

Figure 1. Location map of the 1995 Kozani-Grevena earthquake on a Digital Elevation Model (DEM) built with stereometric SPOT scenes. The star locates the epicentre of the main shock (Hatzfeld *et al.* 1997). The active normal faults are drawn in thin black lines and the thick lines correspond to the faults where surface breaks were observed after the quake (from Meyer *et al.* 1996). The arrows denote artefact areas of the DEM.

The landscape is dominated by the NW–SE trending Hellenic fold thrust belt, with two parallel basins corresponding to broad synclines (Grevena and Kozani) separated by the Vourinos mountain range (Fig. 1) formed of ophiolitic units. Post-Pleistocene deformation is dominated by normal faulting, dipping mainly to the northwest and striking NE-SW, nearly orthogonal to the earlier Hellenic structure. Although this area is characterized by a low historical and instrumental seismicity, morphological evidence of young Quaternary dip-slip faulting is clear along the Servia Fault, with 1000 to 2000 m of structural offset, and along the Paliuria Fault (Meyer *et al.* 1996). The 1995 earthquake did not rupture this well-developed *en echelon* fault system. Meyer *et al.* (1996) reported surface ruptures over 8 km comprising open fissures and scarps of 2–4 cm down-to-the-northwest slip on the pre-existing Palaeochori Fault striking N70°E. At the eastern extremity of the Palaeochori Fault, numerous small slumps over smaller splaying faults indicate that these segments ruptured during the main event (Meyer *et al.* 1996). The surface breaks lie about 15 km south of the epicentre and of the main cluster of aftershocks (Hatzfeld *et al.* 1997). There was no evidence of surface rupture west of the Palaeochori Fault despite the presence of significant aftershock activity.

In a previous paper, Meyer *et al.* (1996) proposed a first-order model of the rupture combining tectonic observations of surface ruptures and SAR interferometry, which consisted of a principal normal dislocation intersecting the surface at the trace of the mapped fault and a minor *en echelon* splay in the eastern part, as required by SAR data. Meyer *et al.*'s model involves faulting down to 15 km depth and yields a total seismic moment of 6.4×10^{18} N m, close to the Harvard CMT estimate of 7.6×10^{18} N m. Although this model satisfactorily explains the available data, some inconsistencies have not so far been discussed. In particular, the complexity of the fault system, with segments changing in strike and dip, is not well described by rectangular dislocations. This approach leads to discontinuities and overlaps along the fault system, producing unrealistic singularities at the edges of the dislocations.

Questions also remain concerning the consistency of this model with seismological data. First, Meyer *et al.*'s model does not cross the main-shock hypocentre. This model also disagrees with those proposed by Clarke *et al.* (1997) and Hatzfeld *et al.* (1997), which are very similar. In both cases, the rupture extends 12–15 km farther to the west without reaching the surface, the surface breaks observed in the field being considered secondary effects of the quake (see comments in Meyer *et al.* 1998; Clarke *et al.* 1998). Some authors, on the basis of aftershocks, have also suggested an antithetic fault dipping to the south, located north of the main rupture which would have been activated during the earthquake (Hatzfeld *et al.* 1997; Chiarabba & Selvaggi 1997; Resor *et al.* 2001; Pollard *et al.* 2001). Though these models account for the position of the main-shock hypocentre, they account for the surface breaks and the fault geometry only poorly. Moreover, none of these models can be reconciled with the ground displacement field depicted by the ERS SAR interferogram (Meyer *et al.* 1998).

To discuss all these problems, we here revisit the model of the $M_s = 6.6$, 1995 Kozani–Grevena earthquake using a smoother fault. Specifically, we processed all the available ERS SAR data including the earthquake date (15 interferograms). Detailed analysis of these data allows the identification and removal of atmospheric artefacts to determine with confidence the geometry of the faults activated during the earthquake and the uncertainties associated with the data set. To take into account the complexity of the fault system, we construct a more realistic fault model with triangular elements allowing smooth fault geometry. We compute the surface displacement field using the Poly3D program (Thomas 1993; Pollard *et al.* 2001). This uses a boundary element method (BEM) in homogeneous elastic half-space. Our methodology consists of three steps. First, we explore the fault geometry with respect to the available data. Second, we hold the fault geometry fixed, and explore the slip direction. Third, we determine the slip distribution by inverting the ground deformation field. We confirm that the earthquake activated a normal fault system with a topographic relief lower than 50 m. This fault is part of a larger *en echelon* system including the Paliuria and Servia faults.

2 SAR DATA PROCESSING

We calculated 15 differential interferograms (Table 1) from nine radar images acquired by the European ERS-1 satellite in C-band (56 mm wavelength) in its descending orbit. The interferograms were computed with the DIAPASON software developed at the French Centre National d'Études Spatiales (CNES) (Massonnet *et al.* 1993). Using a two-pass approach, we corrected the topographic effect using a digital elevation model (DEM) (Massonnet & Feigl 1998). The DEM obtained from a pair of stereometric SPOT scenes was resampled to 80 m by 80 m pixels and has a vertical rms accuracy of 8 m (Fig. 1).

For all interferograms, the altitude of ambiguity (*Ha*) is sufficiently high (more than 120 m, Table 1) with respect to the rms accuracy of the DEM to ensure moderate topographic residuals overall. However, there are small areas in the DEM with spurious elevations (arrows in Fig. 1), most probably due to the presence of clouds on the SPOT scenes. Indeed, the comparison of the DEM with 1/50 000 scaled topographic maps indicates a maximum topographic error of 300 m close to the Palaeochori Fault. These errors might induce localized additional fringes. For example, for an interferogram with

Table 1. The calculated interferograms. Δt is the time delay in days between the acquisition date of the images and the earthquake date; *Ha* is the altitude of ambiguity. The bold rows correspond to the interferograms used for the inversion.

Image 1	Date 1	Image 2	Date 2	Δt (days)	*Ha* (m)	Coherence
5205	19920714	21581	19950831	−1023/+120	−558	30 per cent
5205	19920714	6918	19960816	−1023/+471	−179	5 per cent
5205	19920714	30559	19970522	−1023/+750	−1675	5 per cent
5706	19920818	21581	19950831	−988/+120	−124	30 per cent
5706	19920818	6918	19960816	−988/+471	−256	40 per cent
5706	19920818	30599	19970522	−988/+750	−110	20 per cent
6708	19921027	12219	19931116	−887/−502	479	60 per cent
6708	**19921027**	**22082**	**19951005**	**−887/ + 186**	**−228**	**70 per cent**
6708	19921027	22583	19951109	−887/+221	837	0 per cent
12219	**19931116**	**22082**	**19951005**	**−502/ + 186**	**−155**	**80 per cent**
12219	**19931116**	**22583**	**19951109**	**−502/ + 221**	**−1116**	**80 per cent**
21581	19950831	6918	19960816	+120/+471	−264	10 per cent
21581	19950831	30599	19970522	+120/+750	837	40 per cent
22082	19951005	22583	19951109	+186/+221	179	90 per cent
6918	19960816	30599	19970522	+120/+750	−201	40 per cent

an altitude of ambiguity of 120 m, one fringe is generated if the difference between the altitude in the artefact area of the DEM and the real altitude on the field is at least 120 m. Then, close to the Palaeochori Fault, it is possible for the resulting DEM error to generate two additional fringes on the 12219–22082 interferogram ($Ha =$ 155 m) used by Meyer *et al.* (1996).

As shown in Table 1, the interferograms span various intervals, the shortest being 35 days (22082–22583) and the longest 1173 days, that is 4.8 yr (5205–30599). Eleven interferograms include the date of the earthquake, and four span post-seismic periods. To retrieve a more precise and complete displacement field for inversion, we retained the three interferograms with the best correlation (Table 1, Fig. 2a). Two have an altitude of ambiguity *Ha* of less than 300 m (228 and 155 m respectively), and may contain spurious co-seismic fringes within the DEM error area. Nevertheless, these fringes (at most two) are located in known areas which are small compared with the total area affected by the co-seismic deformation. Their effects on the displacement field are negligible. The third interferogram, with $Ha > 1000$ m, is insensitive to DEM errors. We have therefore not sought to account for the small effects that might have been induced locally, close to the Palaeochori Fault.

3 DATA ANALYSIS AND TROPOSPHERIC CORRECTIONS

The three selected interferograms are shown in Fig. 2(a). They have a very comparable general shape with 11 to 12 concentric fringes, outlining a similar kidney-shaped area of subsidence elongated E–W. On the southern part of all the interferograms, the fringes coincide with the observed ruptures, as mentioned by Meyer *et al.* (1996). They also differ in particular areas and some characteristics have not previously been discussed.

The northern part of the deformed area displays distortions and discontinuities in the fringe pattern (northern inset on Fig. 2a) that have not been analysed before. The origin of these distortions is of particular interest because it may correspond to the activation of an antithetic fault, as proposed by Hatzfeld *et al.* (1997). However, the shape of the feature differs on the three interferograms presented in Fig. 2(a). Undulations can be also observed at the eastern part of the deformed area (eastern inset on Fig. 2a). These features appear to correlate with sharp topographic gradients. This correlation is particularly remarkable on the 35-day post-event interferogram starting 7 months after the quake, presented in Fig. 2(b). This post-event interferogram displays 1.5–2 fringes between the Vourinos summit and the transverse E–W valley north of the Palaeochori Fault. These fringes cannot be related to ground deformation because the 35-day interval is too short to observe any significant post-seismic deformation. It is more likely to be an atmospheric effect correlated with topography as described by various authors (for example, Delacourt *et al.* 1998; Massonnet & Feigl 1998; Cakir *et al.* 2003). Changes in the tropospheric delay between the acquisition dates of the two radar images cause phase shifts that decrease with increasing elevation. Multiplying the topography by a dimensionless scaling factor of -4.5×10^{-5} reproduces the 35-day interferogram satisfactorily (Fig. 2b). The small residuals can be explained by deviations from our assumptions of a homogeneous atmosphere (Delacourt *et al.* 1998). The model fails to reproduce the tropospheric fringes close to the Palaeochori Fault (Fig. 2b) with a difference between the observed and the calculated interferograms of half a fringe, as expected from the DEM errors. Nonetheless, the overall resemblance between the topography-correlated tropospheric artefact and the 35-day interferogram suggests that atmospheric corrections should be applied to the co-seismic interferograms (Fielding *et al.* 1998). We then corrected the three selected interferograms by scaling the DEM by factors of -4.5×10^{-5}, -4.0×10^{-5} and -2.5×10^{-5} respectively to remove most of the artefact fringes (Fig. 2c). In that way, we reduced the differences between each of the three selected interferograms from two to three fringes to one to one and a half fringes.

Next, we unwrapped the phase of each of the three corrected interferograms. Because of the poor radar correlation in the western part of the fringes, the unwrapping software does not resolve the entire deformation field, even when fringes are distinguishable by eye. Then, for each interferogram and for approximately 1500 pixels we digitized the fringes to find the range change (mm) in the ground-to-satellite line of sight (for example, Fig. 3(a) for the 12 219–22 583 interferogram). As can be seen in Fig. 3(a), the limit of null deformation does not appear on the north and on the west edges of the interferogram. This condition represents a lack of constraint in the displacement field for the inversion procedure and will overestimate the slip on the fault. We interpolated these displacements onto a regular grid to define a null deformation zone for the entire area studied (Fig. 3b). The three displacement fields, smoothed with respect to the digitized fringes, were resampled onto a 500 m mesh to reduce the computation time.

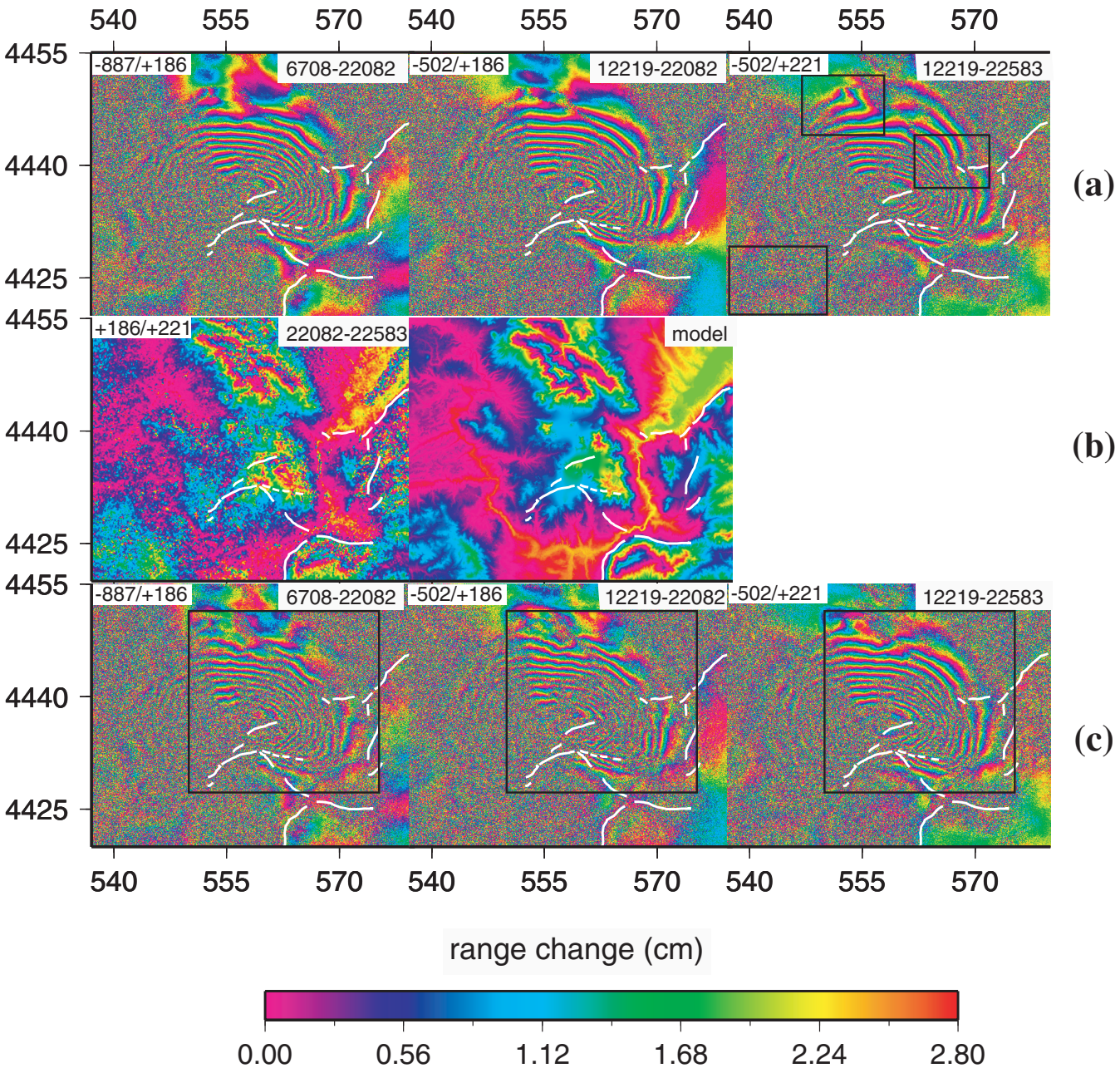

Figure 2. (a) The 6707–22082, 12219–22082 and 12219–22583 co-seismic interferograms (see Table 1 for details). The colour scale corresponds to one fringe, that is 2.8 cm of range change in the ground-to-satellite line of sight. (b) The post-seismic interferogram 22082–22583 over a period of 35 days (left) compared with a tropospheric model (right) obtained by multiplying the digital elevation model by a factor of -4.5×10^{-5}. (c) The same interferograms as (a) with the tropospheric contribution removed in the outlined area (see text for details). Δt, the time delay in days between the acquisition date of the images and the earthquake date, is indicated at the top left corner in each interferogram.

4 MODELLING STRATEGY

To determine the fault model, we followed a three-step strategy, integrating various existing algorithms and combining direct modelling with formal inversion. We first explored the 3-D geometry of the fault system activated. At the surface, these faults follow the mapped surface ruptures and fault scarps identified on SPOT images (Meyer *et al.* 1996). At depth, the only constraint is given by the location of the hypocentre, which should intersect the fault plane. The fault system was subdivided into five subfaults that were subdivided into 1572 triangular elements following the method used by Oleskevich *et al.* (1999). The surface obtained is smooth with gradual changes in strike and dip (Fig. 4). In the second stage, we explored the slip azimuth (rake projection at the surface), fixing it first to the extension direction indicated by the focal mechanism for all the subfaults. This implies small right-lateral components on the western segments and left-lateral components on the eastern ones. The slip direction is progressively changed to fit the pattern of the deformation field. The rakes determined tend to be purely normal on each fault (Fig. 4). Finally, at each change in the fault geometry or slip direction, we estimated the slip distribution using an iterative gradient strategy with least square constraints minimizing the

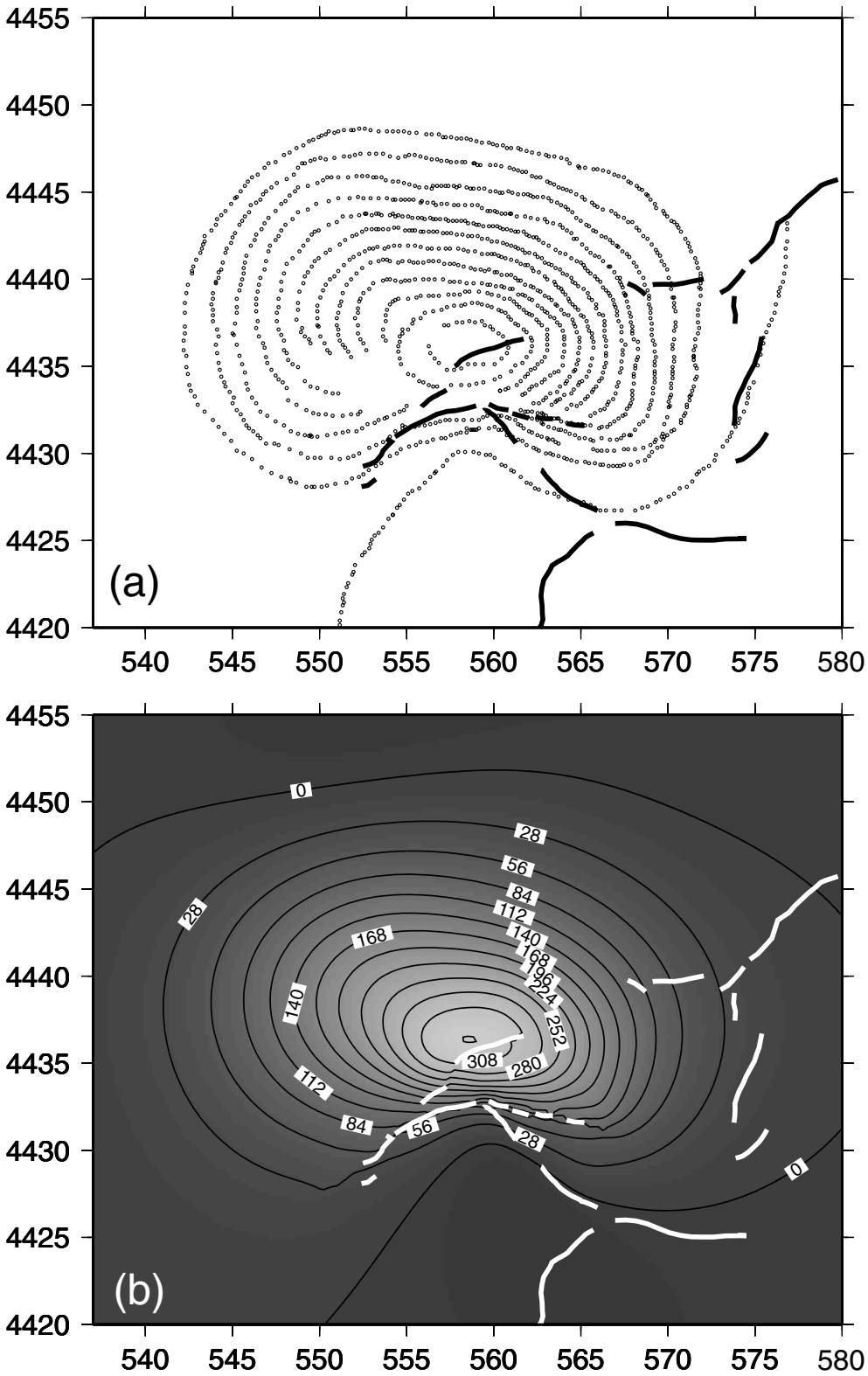

Figure 3. Digitized fringes (a) subsequently interpolated on a regular grid and (b) with the faults drawn for the 12219–22583 interferogram. The numbers correspond to the range change in mm in the ground-to-satellite line of sight.

rms misfit between the observed and calculated range changes. The geometry and the slip azimuth are determined step by step for the three selected interferograms. The only *a priori* constraints are null slip at the surface (first row of triangular elements) for subfaults 2 and 4 in accord with the tectonic observations (Meyer *et al.* 1996). The other triangular patches are free of slip constraints. A map of residuals to be minimized is produced, and the slip distribution is evaluated and analysed.

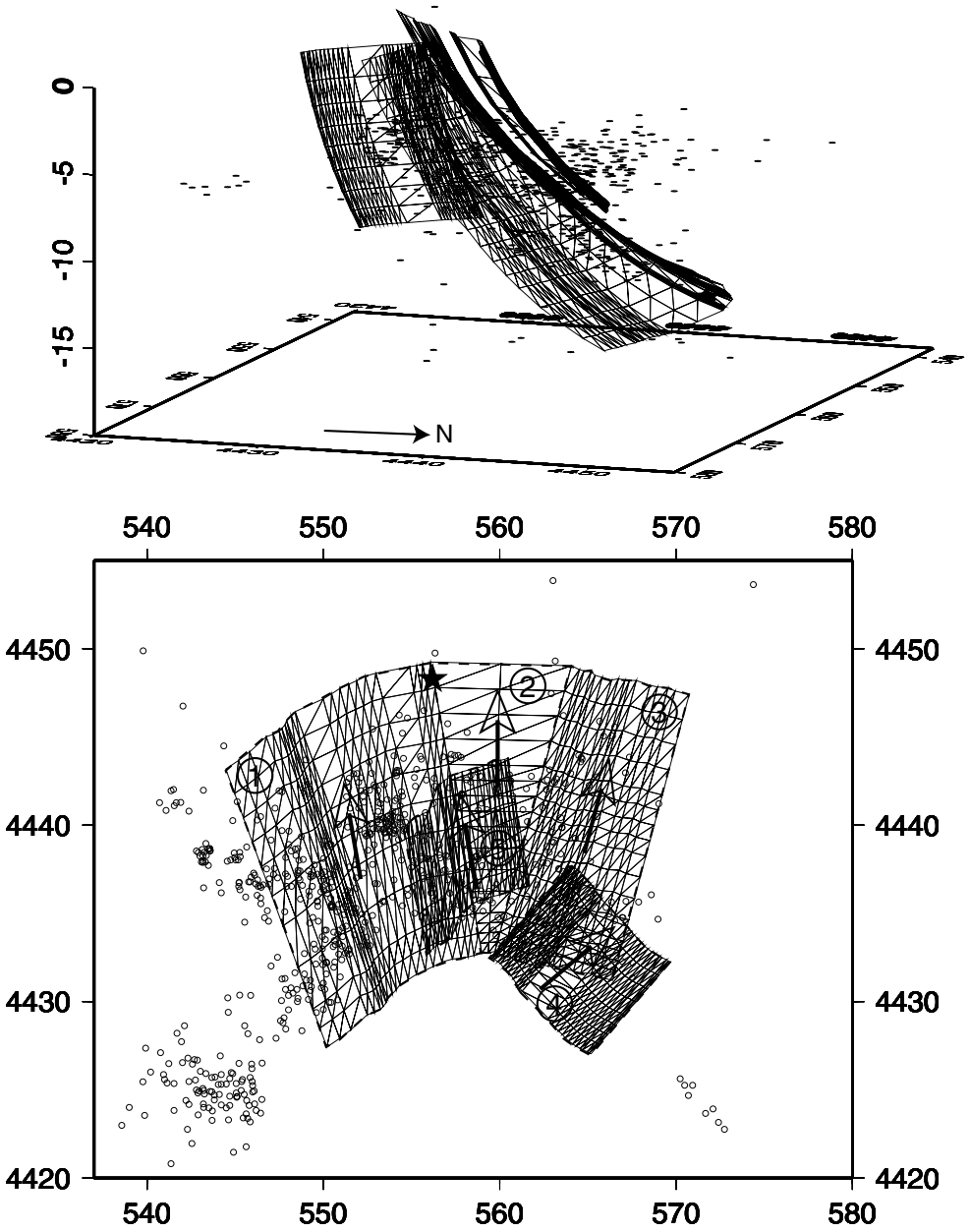

Figure 4. Fault plane model composed of 1572 triangular elements. The aftershocks and the location of the main shock (star) from Hatzfeld *et al.* (1997) are shown. Top, 3-D view from the northeast; bottom, map view; the arrows correspond to the slip azimuth and the numbers to the subfaults described in Table 2.

Table 2. Geometric characteristics of the five subfaults that make up the fault model.

Subfault	Triangles	Area (km^2)	Mean strike (°E)	Mean dip (°)	Slip azimuth (°E)
1	420	266	238	43	350
2	64	90	271	43	0
3	480	159	298	43	15
4	432	91	319	53	50
5	176	84	242	54	350
	1572	690			

Table 3. Inversion results obtained from the three displacement fields retrieved from the three corrected interferograms shown in Fig. 2(c); *Mo* is the scalar seismic moment.

Inverted data	RMS (mm)	Maximum slip (m)	*Mo* (10^{18} N m)
12219–22583	11.7	2.86	7.77
12219–22082	11.4	3.33	8.01
6708–22082	11.4	2.94	7.71

Obviously, these three steps in our modelling strategy are linked because of a trade-off between dip, slip azimuth and slip amplitude. For example, increasing the dip of the fault plane at the surface means that a dip of less than 15° at depth is required to intersect the hypocentre, and the amplitude of slip reaches more than 9 m, which is unreasonable. Conversely, if the dip is decreased at the surface, the fault plane does not pass through the hypocentre.

Constructing the fault model to include the hypocentre and surface breaks, we find our preferred fault geometry as presented in Fig. 4 and Table 2. The fault area is about 691 km^2 and covers most

of the aftershock area. The dip is 65° at the surface, 40° at 9 km depth and 22° at the hypocentre location. Fixing the slip azimuth on all the faults to the rake value deduced from the focal mechanism leads to large residuals because the elliptical shape of the deformed area is larger than observed. At the other extreme, purely normal slip on each subfault fits the observations well. However, the rake cannot be determined with an accuracy better than 15° and there is room for small lateral components on the end of the faults.

5 RESULTS

We obtained three different models, one per input ground deformation, with rms overall misfits of less than 12 mm (Table 3). The maximum slip is 3.0 ± 0.3 m and the scalar seismic moment is 7.8 ± 0.2 10^{18} N m. The maximum slip is always located on the same area of the fault plane at 12.5 km depth; the neighbouring patches have 0.5 m less slip.

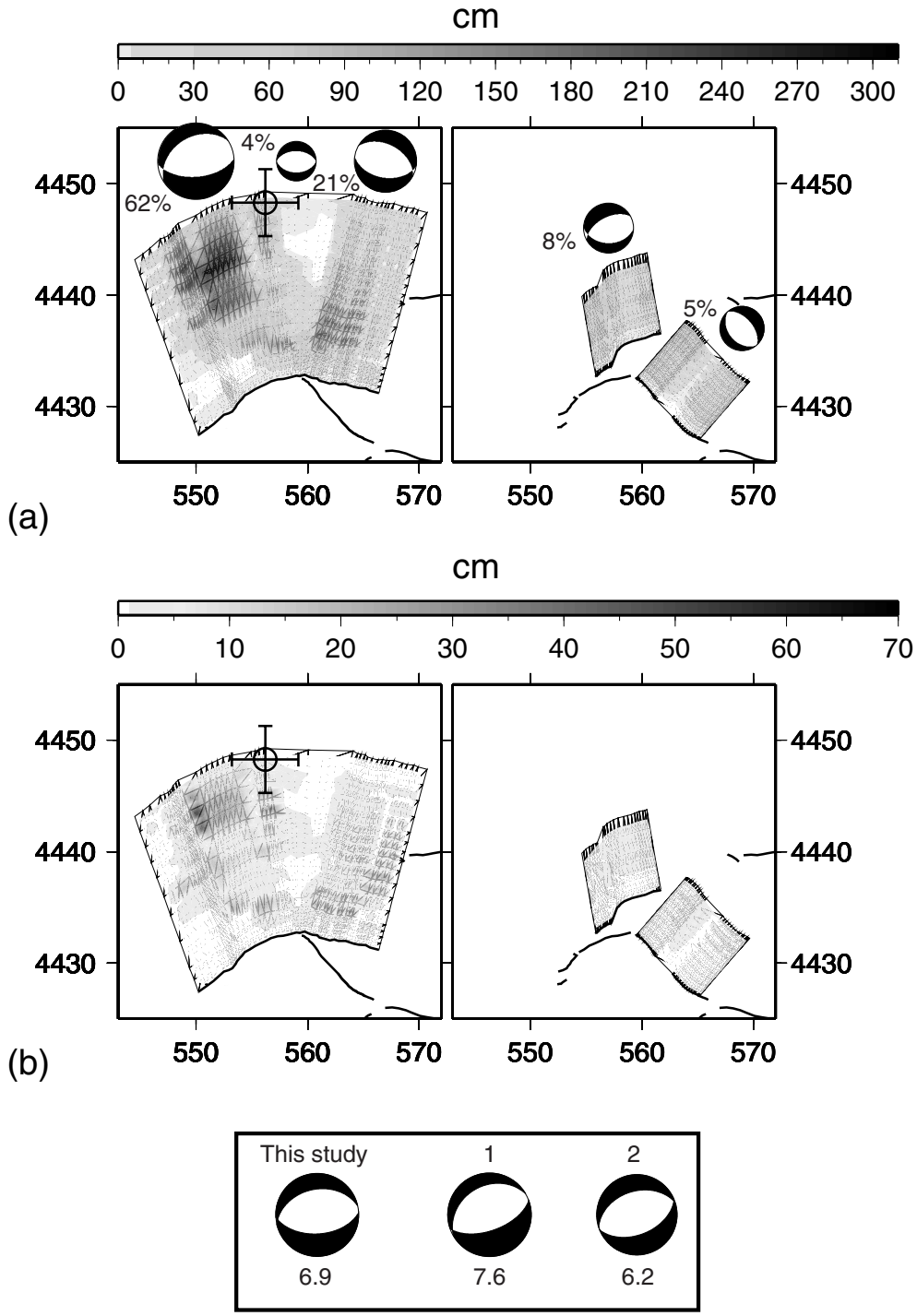

Figure 5. Averaged co-seismic slip distribution model (a) and corresponding standard deviation (b). Focal mechanisms for each subfault are shown. The composite focal mechanism is compared with (1) the Harvard CMT determination and (2) that obtained by Hatzfeld *et al.* (1997), the seismic moment *Mo* (10^{18} N m) being indicated below.

We calculate an average model from these three different models and its associated standard deviation (Fig. 5). The average model exhibits slip values ranging from 0 to 300 cm. The slip at the surface, in those areas where it was not constrained to zero, reaches a value of 4–6 cm for subfault 1, consistent with what was observed in the field by Meyer *et al.* (1996), and 5 cm and 2 cm for subfaults 3 and 5 respectively. This consistency between the estimated and observed slip at the surface gives us confidence in the slip distribution determined at depth. The model shows heterogeneous slip with 80 cm at the nucleation zone of the earthquake, and a fault plane area with a slip of about 2.8 m that was unresolved in the previous models. Subfault 2 shows almost no slip at depth, indicating that the rupture propagated eastward on the shallowest part of the fault. Subfault 3 exhibits high values of slip at 1–1.5 m. The slip on subfaults 4 and 5 is more homogeneous at roughly 80 cm. The standard deviation of the slip amplitude does not exceed 15 cm over most the model, except for the maximum slip area where it reaches a value of 70 cm (Fig. 5). This highest value could be due either to uncorrected tropospheric effects to the north of the deformed area, or to the poorly resolved edges of the null ground deformation zone.

In Fig. 6(c), we show the residuals for the 12219–22583 interferogram obtained by subtracting the synthetic fringes (Fig. 6b)

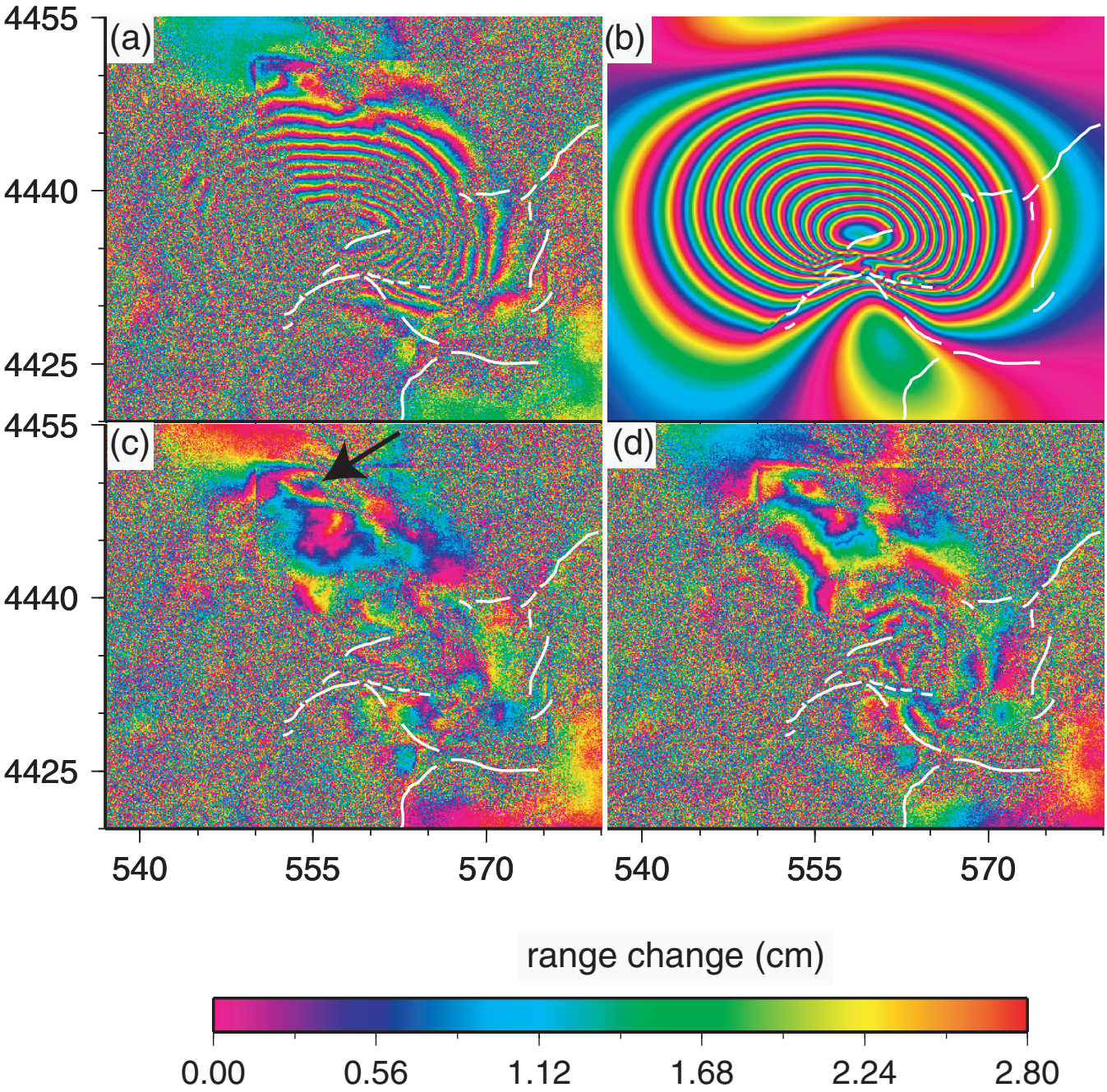

Figure 6. 12219–22583 interferogram: (a) observed and (b) synthetic interferogram obtained from the averaged co-seismic model; (c) residual interferogram obtained by removing (b) from (a)—the arrow indicates the location of a hypothetical antithetic fault (see text for details); (d) residual interferogram obtained by removing the model of Meyer *et al.* (1996) from (a).

Table 4. Parameters of the nodal plane dipping to the north of the focal mechanisms determined for the Kozani–Grevena earthquake.

	Strike (°E)	Dip (°)	Rake (°)
This study	257.8	38.2	−97.1
Harvard CMT	240	31	−90
Hatzfeld *et al.* (1997)	252	41	−87

calculated for the averaged model from the observed one (Fig. 6a). The residuals, at slightly over one fringe over most the interferogram, correspond to atmospheric heterogeneities not accounted for by our correction. For comparison, Fig. 6(d) shows the residuals obtained with the model proposed by Meyer *et al.* (1996). These residuals are more than three fringes due to (1) atmospheric and DEM artefacts, (2) the absence of high slip on the fault at depth and (3) a less precise fault geometry, which generates the NE–SW rectangular fringe pattern in the western part.

Finally, we determined the composite focal mechanism of the averaged model (Fig. 5, Table 4), which differs slightly from that determined by waveform modelling (Hatzfeld *et al.* 1997). The corresponding seismic moment yields $(6.9 \pm 0.5) \times 10^{18}$N m in good agreement with the CMT determination.

6 DISCUSSION AND CONCLUSIONS

We have determined a fault model in agreement with the tectonic and seismological observations that fits the differential InSAR (DInSAR) observations better than previous models.

In our inversion we do not take into account the composite triangulation GPS data of Clarke *et al.* (1997). As discussed by Meyer *et al.* (1998), because the triangulation survey was undertaken in 1984–1986 and the GPS survey just after the quake, these data might include substantial interseismic strain or large errors, such as has been seen in the Gulf of Corinth (Briole *et al.* 2000).

There is an aftershock cluster WSW of the fault (Fig. 4), between 7 km and 10 km depth, including events with strike-slip mechanisms (Hatzfeld *et al.* 1997). This cluster seems to be associated with one circular fringe in the southwestern limit of the elliptical fringe pattern (Figs 2a–c). We did not model this peculiar fringe because of its uncertain origin. It might be due to an uncorrected atmospheric contribution or to human activities such as water pumping for cultivation or to tectonic deformation. Specifically, it is difficult to relate this apparent deformation with the aftershock cluster, which seems to be too deep to generate such a signal. Nevertheless, this feature could be associated with post-seismic shallow processes such as pore fluid transfers in the sedimentary basin in response to high strain accumulation at the end of the co-seismic rupture. Such processes were observed in compressive jogs after the 1992 Landers earthquake (Peltzer *et al.* 1998).

The primary discrepancy between our model and the SAR data is found in the northern part of the deformed area (arrow in Fig. 6c). We explore the possibility that this feature corresponds to secondary faulting during the earthquake, as suggested by various authors from analysis of the aftershock distribution and from local tomography (Hatzfeld *et al.* 1997; Chiarabba & Selvaggi 1997; Resor *et al.* 2001). These residues can be explained by small slip (20 cm) on a shallow fault (0–5 km) extending over 5 km, dipping to the south, and lying north of the Palaeochori Fault where the fringes are distorted. We do not find this argument compelling. First, this model induces an uplift of the northern area, which is not observed on the interferograms. Second, this model implies therefore the presence of a fault that was not observed in the field. Moreover, no indirect evidence for tectonic faulting (such as cracks or slumps) has been mapped there. Since activity on an antithetic fault seems to be incompatible with the SAR and tectonic observations, we attribute the residual fringes to atmospheric effects not accounted for by our corrections.

The most important and robust result is the presence of a fault area of approximately 20 per cent of the main surface fault, with slip reaching 2.8 ± 0.5 m, that corresponds to a zone of low aftershock activity. The model proposed is composed of five subfaults, of which two (1 and 3) account for 80 per cent of the total seismic moment (Fig. 5), of which 85 per cent occurs on the deeper part of subfault 1, indicating that the general trend of the extension in this region is N–S. Moreover, the large area with significant slip corresponds in this activated fault system to the faults with the clearest morphological expression. The Paliuria Fault has a similar geometry but a more prominent morphology than the Palaeochori Fault. The latter might be of younger inception than the former. This may indicate an attempt by the Servia and Palaeochori fault systems to connect across the Vourinos mechanical obstacle, an ophiolite massif where the deformation is more diffuse and not easily localized on faults.

ACKNOWLEDGMENTS

We are grateful to Dimitri Papanastassiou for providing meteorological data, to Denis Hatzfeld for providing the aftershock data, to David Pollard for providing the Poly3D software and to Kurt Feigl for interesting discussions as well as to C. Delacourt, R. Evans and an anonymous reviewer for helpful comments. This work was supported by the French Programme National de Télédétection Spatiale (CNRS/INSU) and the EC Environment Programme (PRESAP).

REFERENCES

Briole, P. *et al.,* 2000. Active deformation of the Corinth rift, Greece: results from repeated Global Positioning System between 1990 and 1995, *J. geophys. Res.,* **105,** 25 605–25 625.

Cakir, Z., de Chabalier, J.B., Armijo, R., Meyer, B., Barka, A. & Peltzer, G., 2003. Coseismic and post-seismic slip associated with the 1999 Izmit earthquake (Turkey), from SAR interferometry and tectonic field observations, *Geophys. J. Int.,* **155,** 93–110.

Chiarabba, C. & Selvaggi, G., 1997. Structural central on fault geometry: example of the Grevena Ms 6.6, normal faulting earthquake, *J. geophys. Res.,* **102,** 22 445–22 457.

Clarke, P.J., Paradissis, D., Briole, P., England, P.C., Parsons, B.E., Billiris, H., Veis, G. & Ruegg, J.C., 1997. Geodetic investigation of the 13 May 1995 Kozani-Grevena (Greece) earthquake, *Geophys. Res. Lett.,* **24,** 707–710.

Clarke, P.J., Paradissis, D., Briole, P., England, P.C., Parsons, B.E., Billiris, H., Veis, G. & Ruegg, J.C., 1998. Reply to the comment on 'Geodetic investigation of the 13 May Kozani-Grevena (Greece) earthquake' by Meyer *et al., Geophys. Res. Lett.,* **25,** 131–133.

Delacourt, C., Briole, P. & Achache, J., 1998. Tropospheric corrections of SAR interferograms with strong topography. Application to Etna, *Geophys. Res. Lett.,* **25,** 2849–2852.

Feigl, K.L., Sergent, A. & Jacq, D., 1995. Estimation of an earthquake focal mechanism from a satellite radar interferogram: application to the December 4, 1992 Landers aftershock, *Geophys. Res. Lett.,* **22,** 1037–1040.

Feigl, K. *et al.,* 2002. Estimating slip distribution for the Izmit mainshock from coseismic GPS, SPOT, and ERS-1 measurements, *Bull. seism. Soc. Am.,* **92,** 138–160.

Fielding, E.J., Blom, R.G. & Goldstein, R.M., 1998. Rapid subsidence over oil fields measured by SAR interferometry, *Geophys. Res. Lett.,* **25,** 3215–3218.

Hatzfeld, D. *et al.,* 1997. The Kozani-Grevena (Greece) earthquake of 13 May 1995 revisited from a detailed seismological study, *Bull. seism. Soc. Am.,* **87,** 463–473.

Hernandez, B., Cotton, F. & Campillo, M., 1999. Contribution of radar interferometry to a two-step inversion of the kinematic process of the 1992 Landers earthquake, *J. geophys. Res.,* **104,** 13 083–13 099.

Massonnet, D. & Feigl, K.L., 1998. Radar interferometry and its application to changes in the Earth's surface, *Rev. Geophys.,* **36,** 441–500.

Massonnet, D., Rossi, M., Carmona, C., Adragna, F., Peltzer, G., Feigl, K. & Rabaute, T., 1993. The displacement field of the Landers earthquake mapped by radar interferometry, *Nature,* **364,** 138–142.

Massonnet, D., Feigl, K., Rossi, M. & Adragna, F., 1994. Radar interferometric mapping of deformation in the year after the Landers earthquake, *Nature,* **369,** 227–230.

Meyer, B. *et al.,* 1996. The 1995 Grevena (Northern Greece) earthquake: fault model constrained with tectonic observations and SAR interferometry, *Geophys. Res. Lett.,* **23,** 2677–2680.

Meyer, B., Armijo, R., Massonnet, D., de Chabalier, J.B., Delacourt, C., Ruegg, J.C., Achache, J. & Papanastassiou, D., 1998. Comment on 'Geodetic investigation of the 13 May Kozani-Grevena (Greece) earthquake' by Clarke *et al., Geophys. Res. Lett.,* **25,** 129–l30.

Oleskevich, D.A., Hyndman, R.D. & Wang, K., 1999. The updip and downdip limits to great subduction earthquakes: thermal and structural models of Cascadia, south Alaska, SW Japan and Chile, *J. geophys. Res.,* **104,** 14 965–14 991.

Peltzer, G., Rosen, P. & Ragez, F., 1998. Poroelastic rebound along the Landers 1992 earthquake surface rupture, *J. geophys. Res.,* **103,** 30 131–30 145.

Pollard, D., Maerten, F., Maerten, L., Resor, P., Muller, J. & Aydin, A., 2001. Improved 3D modeling of complex fault geometries using Poly3D, an elastic boundary element code, *EOS Trans. AGU,* **82**(47), Fall Meet. Suppl., Abstract S21B-0572.

Resor, P.G., Beroza, G.C. & Pollard, D.D., 2001. Imaging fault structure of the 1995 Kozani-Grevena earthquake sequence, Greece, using high precision aftershock locations, *EOS Trans. AGU,* **82**(47), Fall Meet. Suppl., Abstract G31B-0143.

Thomas, A.L., 1993. Poly3D: a three-dimensional, polygonal element, displacement discontinuity boundary element computer program with applications to fractures, faults and cavities in the Earth's crust, M.S. Thesis, Stanford University, CA.

Wright, T., Parsons, B. & Fielding, E., 2001. Measurement of interseismic strain accumulation across the North Anatolian Fault by satellite radar interferometry, *Geophys. Res. Lett.,* **28,** 2117–2120.